

Deep priors for satellite image restoration with accurate uncertainties *

Maud Biquard
ISAE-Supaero / CNES
31400 Toulouse, France

maud.biquard@isae-supaero.fr

Florence Genin, Christophe Latry
CNES

31400 Toulouse, France

firstname.lastname@cnes.fr

Marie Chabert
IRIT/INP-ENSEEIH
31000 Toulouse, France

marie.chabert@toulouse-inp.fr

Thomas Oberlin
ISAE-Supaero
31400 Toulouse, France

thomas.oberlin@isae-supaero.fr

Abstract

Satellite optical images, upon their on-ground receipt, offer a distorted view of the observed scene. Their restoration, classically including denoising, deblurring, and sometimes super-resolution, is required before their exploitation. Moreover, quantifying the uncertainty related to this restoration could be valuable by lowering the risk of hallucination and avoiding propagating these biases in downstream applications. Deep learning methods are now state-of-the-art for satellite image restoration. However, they require to train a specific network for each sensor and they do not provide the associated uncertainties. This paper proposes a generic method involving a single network to restore images from several sensors and a scalable way to derive the uncertainties. We focus on deep regularization (DR) methods, which learn a deep prior on target images before plugging it into a model-based optimization scheme. First, we introduce VBLE-xz, which solves the inverse problem in the latent space of a variational compressive autoencoder, estimating the uncertainty jointly in the latent and in the image spaces. It enables scalable posterior sampling with relevant and calibrated uncertainties. Second, we propose the denoiser-based method SatDPIR, adapted from DPIR [73], which efficiently computes accurate point estimates. We conduct a comprehensive set of experiments on very high resolution simulated and real Pléiades images, asserting both the performance and robustness of the proposed methods. VBLE-xz and SatDPIR achieve state-of-the-art results compared to direct inversion methods. In particular, VBLE-xz is a scalable method to get realistic posterior samples and accurate uncertainties, while SatDPIR represents a compelling alternative to direct inversion methods when uncertainty quantification is not required.

1 Introduction

Satellite imaging is of considerable interest for various remote sensing applications such as environmental monitor-

ing, conservation programs, or urban planning. Some satellite optical systems can now acquire images at a very high resolution. For instance, a PLEIADES-HR satellite captures images in which each pixel represents a $70\text{cm} \times 70\text{cm}$ area on the ground and is coded in 12 bits. This allows for a detailed visualization of the Earth surface and provides extremely valuable information for object detection [27, 10], change detection, or semantic segmentation [69, 4]. However, despite constant technological advances in sensor accuracy, satellite images provide an imperfect representation of the observed scene. In particular, the images contain noise and blur induced by the optical system, satellite movement, atmospheric perturbations, and onboard compression. As a consequence, the received image must be restored to get the most out of its on-ground exploitation. The restoration aims at enhancing the image quality by removing the noise and blur mentioned above. Additional processing, such as super-resolution, can also be applied to ease data interpretation for downstream tasks. All these processes must preserve the integrity of the information: no information should be removed and no false details added. Furthermore, the restoration process has to remain computationally viable to treat the important amount of data transmitted on the ground. Finally, the restoration process should ideally be sufficiently generic to process images from different satellites.

We restrict our study to panchromatic images, which offer the highest spatial resolution. They can be combined with multi-spectral images of lower resolution through panchromatic sharpening to obtain high resolution multispectral images. The acquisition of a panchromatic image by the satellite optical system can be modelled as

$$y = \mathcal{D}_0(h_0 * s) + w, \quad (1)$$

where s represents the observed landscape, y the acquired

*This work was partly supported by CNES under project name DEEP-REG, and ANITI under grant agreement ANR-19-PI3A-0004.

image, $h_0 = h_{atmo} * h_{move} * h_{ins}$ models the combined effects of the atmosphere, of the movement during integration time, and of the instrument. \mathcal{D}_0 denotes the sampling operator. Vector w represents a white Poisson-Gaussian noise which can, for the considered problems, be approximated by a Gaussian noise of variance $\sigma_w^2(s) = \sigma_0^2 + K\mathcal{D}_0(h_0 * s)$, where σ_0 and K are noise parameters specific to a given optical system. Current Pléiades image restoration processes [40] employ traditional methods such as NL-Bayes for denoising [42] and inverse filtering for deconvolution [40]. However, these methods require *ad hoc* operations to stick to the white Gaussian noise model favorable to NL-Bayes denoiser [49]. Moreover, since the advent of deep learning, they are not anymore state-of-the-art for image restoration.

Indeed, deep learning has led to a substantial breakthrough in image restoration [73, 79]. A first category of methods, which we denote by direct inversion methods in the sequel, learns a neural network that maps the degraded image to the restored image in a supervised manner [79, 68, 66]. However, as they learn a specific mapping for each forward model defined by (1), a neural network must be learned for each sensor. A second category of methods, which we call deep regularization (DR) methods in the following, merely learns a regularization independently of the forward model (1) from a dataset of target images, that is the original landscapes downsampled at a target resolution. While plug-and-play (PnP) approaches learn an implicit regularization within a denoiser [73, 64, 31, 34], latent optimization methods regularize explicitly the inverse problem, by looking for the problem solution in the latent space of a generative model [6, 5, 56]. DR methods typically compute the Maximum A Posteriori (MAP) estimate:

$$\max_x p_{X|Y}(x|y) \Leftrightarrow \min_x -\log p_{Y|X}(y|x) - \log p_X(x) \quad (2)$$

where x is the current estimation of the target image, y is the measured image, $p_{Y|X}(y|x)$ is the data likelihood, $p_{X|Y}(x|y)$ the inverse problem posterior. The regularization $-\log p_X(x)$ promotes solutions of the inverse problem most compatible with the prior $p_X(x)$, which is learnt beforehand from a dataset of target images. A first benefit is that a single neural network is trained once to perform different restoration tasks for different sensors or different acquisition conditions, in the spirit of foundation models. A second benefit is that DR methods, unlike direct inversion approaches, can use standard denoisers or generative models, for which models pretrained on large databases are available. Hence, using them for satellite restoration only requires their finetuning on a smaller database of target satellite images. Then, DR methods rely on an optimization process often similar to eq. (2), which allows to control the strength of the regularization during the optimization process, for instance with a classical regularization parameter. This helps to remain faithful to the measure, which is cru-

cial for satellite image restoration.

Last but not least, some DR methods do not only estimate the MAP, but enable to sample from the posterior distribution $p_{X|Y}(x|y)$. This remarkably allows to derive uncertainties, which are valuable for downstream applications. However, these methods are often computationally expensive as they mainly rely on Monte Carlo Markov Chains (MCMC) sampling. Yet, in Biquard et al. [5], we have proposed another method for approximate posterior sampling, called Variational Bayes Latent Estimation (VBLE), relying on latent optimization with a variational compressive autoencoder. VBLE allows for approximate posterior sampling with no significant increase in computational cost, and seems well suited for remote sensing image restoration.

However, while direct inversion methods are more and more studied in the context of remote sensing, and even used in real on-ground segments [81, 12], DR methods have rarely been considered in the literature. This paper aims at filling this gap, by demonstrating the interest of DR for remote sensing image restoration. In particular, we will show that DR methods can reach similar or even better performance than inversion-based techniques, and with the extra ability to predict an accurate estimation of the uncertainties. Although they require in general more computation, this remains scalable in a real context. And since they can be easily adapted to any sensor or acquisition conditions without any re-training, we believe they can even be easier to use in real on-ground segments.

Our contributions are the following:

- We propose an improved version of VBLE, called VBLE-xz, which yields more informative uncertainties by taking into account the reconstruction error of the generative model. We also adopt a calibration strategy, so that our method provides state-of-the-art results with accurate perpixel error bounds in a reasonable amount of time.
- We also propose SatDPIR, an adaptation of the state-of-the-art PnP method Deep Plug-and-play Image Restoration (DPIR) [73] to the specific noise model encountered in satellite imaging. SatDPIR allows for fast and accurate satellite image restoration and can be advantageously used when uncertainties are not required.
- We conduct a comprehensive set of experiments on high resolution satellite images simulated in a realistic manner, as well as on real satellite images to show the interest of these two DR methods. We show their interest over alternative DR techniques. Furthermore, we also compare our methods to direct inversion in terms of performance and robustness, showing that they yield similar metrics as direct inversion methods, but with fewer artefacts and improved robustness to modelling errors.

2 Related works

2.1 Image restoration techniques

Image restoration is a well-known inverse problem, which has classically been addressed using variational methods. The key point of these methods, which consist in minimizing a functional composed of a data fidelity term and of a regularization term such as in eq. (2), is to choose a proper regularization. Classical regularizations include total variation [57], Tikhonov regularization [63], and sparsity-promoting penalties on well-chosen representations such as wavelet bases or dictionaries [62, 21, 50]. Recently, deep learning based methods have emerged as a powerful alternative to these classical methods. Direct inversion methods, which directly learn a mapping from the degraded image to the restored image using a neural network, are widespread in image restoration. They commonly use convolution neural networks (CNNs) within either a U-Net architecture [68, 71, 48], or a ResNet architecture [74, 43, 66]. Generative Adversarial Networks (GANs) have been also used to improve perceptual performance [43, 66]. Recently, transformer-based method have enabled better results [68, 70, 44], as well as diffusion-based methods [47, 48], yet at the cost of an increased computational complexity.

Unlike direct inversion methods, DR methods learn only the regularization term, with the help of denoisers or diffusion models in PnP methods [64], or with generative models such as Variational Autoencoders (VAEs) [38] or GANs [26] for latent optimization methods. PnP methods, which yield state-of-the-art results on a wide variety of inverse problems, consist in using splitting algorithms, such as Alternating Direction Method of Multipliers (ADMM) [64, 9] or Half Quadratic Splitting (HQS) [73, 31], that separately handle the data term and the regularization term in the optimization problem. Their key concept is to use Gaussian denoisers [35], and in particular deep denoisers [75] in place of the proximal operator of the regularization. Recently, the use of denoising diffusion models [28] has led to remarkable results for solving imaging inverse problems [36, 13, 82].

While PnP methods implicitly learn the regularization through the denoising process, latent optimization methods represent a more direct way to regularize inverse problems by estimating the data distribution within generative models. The seminal work [6] seeks the inverse problem solution in the latent space of a VAE or a GAN, by optimizing a functional, leading to a latent MAP estimate. Then, the solution is taken as the image generated from the latent MAP. This approach is interesting because of its explicit formulation as well as its well-defined Bayesian framework. However, it suffers from its dependency to the quality of the generative model since the obtained solution necessarily

lies in the generator range. To tackle this problem, [15, 14] permit small deviations from the generative manifold while [25, 18, 19] propose to jointly optimize x and z using splitting algorithms. More recently, in [5], we proposed to replace the generative model by a compressive autoencoder, which can generate a wide variety of images while efficiently regularizing the inverse problem in the latent space through its hyperprior.

While most of the methods described above only provide a single point estimate to the inverse problem, many applications, particularly in Earth observation, require an estimation of the confidence in this solution. To this end, several Bayesian methods enable to sample the posterior distribution $p_{X|Y}(x|y)$ of the inverse problem solution. Some methods yield stochastic solutions to the inverse problem, relying, for instance, on the implicit prior provided by Gaussian denoisers [34] or exploiting diffusion model properties [82]. Another type of method uses Markov Chain Monte Carlo (MCMC) to sample from the true posterior. In particular, [20] proposes to use Unadjusted Langevin Algorithm (ULA) to solve imaging inverse problems. Building on this, PnP-ULA [41] approximates the log-likelihood gradient in ULA by employing a Gaussian denoiser in a PnP framework. Interestingly, [29] attempts to combine MCMC with latent optimization methods by designing a MCMC sampling scheme in the latent space of a generative model. These approaches enable to sample from the true posterior but require a lot of iterations to converge, making them hardly scalable for satellite imaging. In [5], we introduced the VBLE algorithm, performing variational inference in the latent space of a compressive autoencoder. With negligible additional computation cost compared to the deterministic algorithm, VBLE represents a relevant alternative to MCMCs for posterior sampling.

2.2 Application to satellite optical imaging

Once transmitted to the ground station and decompressed, satellite images are subject to an in-depth semantic analysis including for instance perpixel classification [69, 4], object detection [27, 10], or 3D reconstruction [22]. Previously, satellite images must be restored and eventually super-resolved. Most of the deep learning currently used methods are based on direct inversion. For satellite single image super-resolution (SISR) tasks, CNN-based methods [72, 45, 55, 23] and GAN-based methods [7, 33] are widely used. In particular, [81, 12] employ a SRRResNet architecture for joint denoising, deblurring, and super-resolution of optical satellite images. Furthermore, [30] proposes a deep pansharpening network, and [77, 80] perform deep hyper-spectral super-resolution.

Concerning DR methods, PnP methods are commonly used for hyperspectral image processing tasks. For instance, [65, 39] use ADMM PnP framework for hyperspectral im-

age restoration, and [61] for hyperspectral image sharpening. To process panchromatic or multispectral satellite images, [46] employs ADMM for pansharpening, while [60] employs DPSR algorithm [76] for super-resolution. Up to our knowledge, PnP methods have not been commonly used for high resolution satellite image restoration. Concerning latent optimization methods, they have been successfully applied to medical imaging [19]. However, due to the complexity of using these methods on complex datasets, they have not been yet applied to satellite imaging.

For satellite image restoration and super-resolution, the training data are crucial as the network has to generalize to real satellite data. Yet, getting realistic target images, or pairs of degraded and target images for training is challenging. Indeed, obtaining a proper target image requires to downsample an original acquired image by a sufficient factor to neglect the original acquisition effects. Thus, it is common [45, 7, 33] to perform super-resolution at an unrealistic resolution, by considering the satellite image as the target and downsampling it with bicubic kernel to get the low resolution image. [55] employ Sentinel-2 images at a resolution of 10m as high resolution targets to super-resolve Landsat-5 images, which are at 30m resolution. In a similar way, [59] uses Sentinel-2 images as input and Worldview images downsampled at a resolution of 2m as outputs, while [24] learns to map Sentinel-2 images to RapidEye images at a resolution of 5m. For these approaches, the datasets are very limited, as the landscape and season should match for both satellites. [51] presents an open-data licensed dataset composed of 10m and 20m surface reflectance patches from Sentinel-2, with their associated 5m patches acquired by the VEN μ s satellite on the same day. Interestingly, [81, 12] simulate realistic target and degraded images from aerial images that were originally at an extremely high resolution. They respectively use Google and Airbus owned aerial images, which are typically at a resolution lower than 10cm.

3 SatDPIR: An adapted plug-and-play algorithm for satellite image restoration

3.1 Background on DPIR

DPIR [73] is a PnP algorithm relying on Half Quadratic Splitting (HQS). Its particularly low number of iterations as well as its convenient parameter tuning have made DPIR a reference PnP method for solving inverse problems with white Gaussian noise.

Considering a forward model $y = Ax + w$ with A the degradation operator, for instance a convolution, and a white Gaussian noise $w \sim \mathcal{N}(0, \sigma^2)$, DPIR seeks to minimize $\frac{1}{2\sigma^2} \|y - Ax\|^2 + \lambda R(x)$ with respect to x where R is a regularization term. HQS algorithm consists of the fol-

lowing splitting:

$$\min_{x,u} \frac{1}{2\sigma^2} \|y - Ax\|^2 + \lambda R(u) + \frac{\mu}{2} \|u - x\|^2, \quad (3)$$

with u an auxiliary variable that is jointly optimized with x . This leads to an alternate optimization scheme

$$x_k = \arg \min_x \frac{1}{2\sigma^2} \|y - Ax\|^2 + \frac{\mu}{2} \|x - u_{k-1}\|^2, \quad (4)$$

$$u_k = \arg \min_u \frac{1}{2\sqrt{\lambda/\mu}} \|u - x_k\|^2 + R(u). \quad (5)$$

Equation (4) is a proximal step on the data fidelity which can be computed in closed form for various inverse problems. Equation (5) amounts to a denoising step with noise level $\sigma_d = \sqrt{\lambda/\mu}$. [73] proposes to use decreasing values of σ_d , evenly spaced in log scale from σ_1 to $\sigma_2 < \sigma_1$ over the iterations. $\sigma_2 = \sigma$ corresponds to the noise level in the measurement, while $\sigma_1 > \sigma$ is a hyperparameter that is typically set to 50/255 for 8 bits images. With λ a fixed regularization parameter, this leads to a larger $\mu = \frac{\lambda}{\sigma_d^2}$ at each iteration. Note that the number of iterations is fixed *a priori* because of the noise schedule. This results in a very fast convergence, generally within 8 iterations. In [73], the successive denoising steps are performed with DRUnet denoiser as it can manage different noise levels.

3.2 Proposed DPIR adaptation

DPIR algorithm has been specifically designed for inverse problems with white Gaussian noise of fixed variance. Yet, in the forward model (1) considered for satellite image restoration, the acquisition noise is Gaussian but with a spatially varying variance $\sigma_w^2(x) = \sigma_0^2 + K(h_0 * x)$. The associated data likelihood substantially complicates the problem resolution. In particular, the proximal step of eq. (4) can no longer be computed in closed form. This significantly slows down the algorithm convergence for large images, such as satellite ones. To overcome this limitation, we propose in this section a smart initialization of the proximal gradient descent that considerably speeds up its convergence.

First, for the considered inverse problem, the quadratic data fidelity term in equations (3) and (4) should be replaced by the real negative log-likelihood:

$$-\log p_{Y|X}(y|x) \propto \frac{1}{2} (y - h_0 * x)^T \Sigma_w(x)^{-1} (y - h_0 * x) + \frac{1}{2} \log |\Sigma_w(x)| \quad (6)$$

up to a constant, with $\Sigma_w(x) = \text{diag}(\sigma_w^2(x))$. Thus, we replace eq. (4) with:

$$x_k = \arg \min_x -\log p_{Y|X}(y|x) + \frac{\mu}{2} \|x - u_{k-1}\|^2. \quad (7)$$

We adapt the noise schedule by considering $\sigma_2 = \sqrt{a}$, that is the minimum level of noise in the image, and σ_1 is empirically reduced to 20/255, which corresponds to 320/4095 for 12-bit images, as the considered noise levels for satellite imaging is much smaller than classically considered noise levels.

Then, eq. (7) can no longer be expressed in closed form, and should be computed using gradient descent. We propose to initialize the gradient descent at iteration k with

$$x_k^{(0)} = \arg \min_x \frac{1}{2\bar{\sigma}^2} \|y - h_0 * x\|^2 + \frac{\mu}{2} \|x - u_{k-1}\|^2 \quad (8)$$

where $\bar{\sigma}^2 = a + b(h_0 * \bar{u}_{k-1})$ and \bar{u}_{k-1} is the mean value of u_{k-1} . Equation (8), which corresponds to the proximal operator considering a fixed noise level $\bar{\sigma}^2$, can be computed in closed form. Then, we consider two phases during DPIR iterations. During the first half of the iterations, where each iteration corresponds to significant changes in x_k , we do not perform gradient descent on eq. (8) but only the proximal step eq. (8), that is $x_{k-1} = x_{k-1}^{(0)}$. Indeed, we consider $x_k^{(0)}$ to be a sufficiently good approximation to x_k in this case. During the second half of the iterations, we perform gradient descent on eq. (7) starting from $x_k^{(0)}$ during only 5 iterations. We show in the experiments section that this optimization strategy produces very similar results as the original process while being much faster.

4 Variational Bayes joint latent-image estimation with accurate uncertainties

4.1 Variational and compressive autoencoders

Variational autoencoders (VAEs) are generative neural networks, with a decoder D_θ learning a generative latent model and an encoder E_ϕ approximating the generative posterior distribution. Considering the following generative model:

$$p_\theta(x, z) = p_\theta(x|z)p_\theta(z), \quad (9)$$

$p_\theta(z)$ is a latent prior, often assumed to be $\mathcal{N}(0, I)$, while $p_\theta(x|z)$ represents the distribution learned by the decoder. The posterior distribution

$$p_\theta(z|x) = \frac{p_\theta(x|z)p_\theta(z)}{\int_z p_\theta(x|z)p_\theta(z)} \quad (10)$$

is often intractable, and is approximated by $q_\phi(z|x)$, the encoder distribution.

The weights θ and ϕ are learned during the training of the VAE by maximizing the Evidence Lower Bound (ELBO):

$$\mathbb{E}_{q_\phi(z|x)} [\log p_\theta(x|z)] - \text{KL}(q_\phi(z|x) || p_\theta(z)) \quad (11)$$

where KL denotes the Kullback-Leibler divergence between two distributions. In this paper, we consider

$p_\theta(x|z) = \mathcal{N}(D_\theta(z), \Sigma_\theta(z))$, where $\Sigma_\theta(z)$ can be fixed, or learned. In classical VAEs, it is often assumed that $\Sigma_\theta(z) = \gamma^2 I$ and $q_\phi(z|x) = \mathcal{N}(\mu_\phi(x), \text{diag}(\sigma_\phi(x)^2))$. In this case, maximizing the ELBO amounts to minimizing the loss

$$\mathcal{L}(\theta, \phi, \gamma; x) = \mathbb{E}_{q_\phi(z|x)} \left[\frac{1}{2\gamma^2} \|x - D_\theta(z)\|_2^2 \right] + \text{KL}(q_\phi(z|x) || p_\theta(z|x)). \quad (12)$$

Hence, the VAE loss is composed of a data fidelity term and a KL divergence term, which constrains the distribution over the latent space. The parameter γ tunes the trade-off between these two terms and can be either fixed or learned jointly.

Compressive autoencoders (CAEs) are neural networks used for compression, which present similarities with VAEs. CAEs are trained by optimizing the so-called rate distortion trade-off $\mathcal{L} = \text{Rate} + \alpha \times \text{Distortion}$. The distortion represents an error between the input and output of the CAE, and the rate measures the compression efficiency. CAEs can be expressed as VAEs with specific inference and generative distributions [2]. In particular, the encoder posterior $q_\phi(z|x)$ is a uniform distribution, of mean \bar{z} and with a fixed variance in order to simulate the quantization process. Compared to VAE loss, the distortion resembles the data fidelity term, while the rate corresponds to the latent constraint. The trade-off parameter α plays a similar role as γ for VAEs, controlling the trade-off between the two loss terms.

Besides, state-of-the-art CAEs use an hyperprior module [2, 3, 11], as described in Fig. 1. This additional autoencoder takes \bar{z} as input and predicts z 's mean μ^z and deviation σ^z . The latent prior on z is then defined as the factorized distribution $\prod_k \mathcal{N}(\mu_k^z, (\sigma_k^z)^2)$. Hence, the latent prior is a z -adaptive distribution, more powerful and flexible than the traditional VAE prior $\mathcal{N}(0, I)$. Formally, these CAEs can be expressed as VAEs with two latent variables z and h [3].

4.2 Background on VBLE with CAEs

Variational Bayes Latent Estimation (VBLE) [5] is an algorithm used for image restoration, which enables efficient approximate posterior sampling. It belongs to latent optimization methods [6], which estimate the solution of an inverse problem in the latent space of a generative model. In place of a classical generative model, [5] proposed to use CAEs trained on image compression tasks.

Furthermore, the VBLE method estimates the latent inverse problem posterior $p_{Z|Y}(z|y)$ in the latent space of the CAE using variational inference. Specifically, it considers

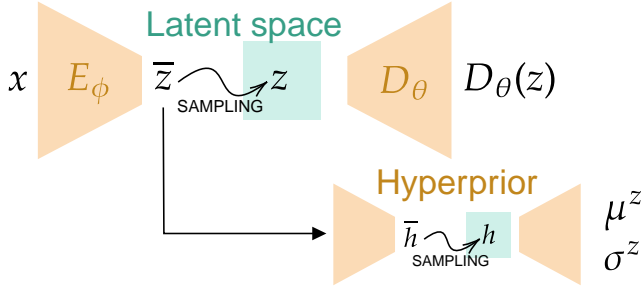


Figure 1. A compressive autoencoder (CAE) with a hyperprior.

the following factorized parametric family:

$$E_{\bar{z},a} = \{q_{\bar{z},a}(z) | \bar{z}, a \in \mathbb{R}^{C \times M \times N}, a > 0\} \quad (13)$$

$$\text{with } q_{\bar{z},a}(z) = \prod_k \mathcal{U}(z_k; [\bar{z}_k - \frac{a_k}{2}, \bar{z}_k + \frac{a_k}{2}])$$

with C , M , and N being the channel and spatial dimensions of the latent space. The parametric distribution $q_{\bar{z},a}$ is chosen to be uniform as it imitates the CAE encoder posterior $q_\phi(z|x)$. Parameters (\bar{z}, a) are classically optimized using variational inference by minimizing $\text{KL}(q_{\bar{z},a} || p_{Z|Y})$. It amounts to maximizing the corresponding ELBO:

$$\mathcal{L}(\bar{z}, a; y) = \mathbb{E}_{q_{\bar{z},a}(z)} [\log p_{Y|Z}(y|z) + \log p_\theta(z) - \log q_{\bar{z},a}(z)] \quad (14)$$

where $p_\theta(z)$ is the latent prior, that is the hyperprior $\mathcal{N}(\mu^z, \sigma^z)$ in the case of CAEs, with the notation of Fig. 1. Using the reparameterization trick $z = \bar{z} + au$ with $u \sim \mathcal{U}(-\frac{1}{2}, \frac{1}{2})$ [38], eq. (14) can be optimized with a Stochastic Gradient Variational Bayes (SGVB) algorithm [37].

4.3 Limitation of latent posterior estimation

VBLE with CAEs [5] enables efficient posterior sampling. Therefore, it seems of great interest for satellite image restoration as employing heavier methods would hardly be scalable. However, having reliable uncertainties is necessary if these are to be used in practical applications.

In our experiments, VBLE tends to underestimate uncertainties. To illustrate this, the first line of Tab. 1 provides confidence interval prediction probabilities (ICP) at level 95% using VBLE with a simple VAE on CelebA. Precisely, for each pixel of an image, we compute a confidence interval of a given level using 100 posterior samples. Then, ICP denotes the proportion of the ground truth pixels lying in the predicted intervals. Table 1 first line shows too low ICPs indicating that uncertainty predictions could be improved.

Yet, in latent optimization methods, there are three types of errors [6]: the optimization error, the inverse problem error (caused by the inverse problem's ill-posedness), and the

	$\sigma = 2.55/255$	$\sigma = 7.65/255$
CelebA	0.84	0.93
ManifoldCelebA	0.92	0.96

Table 1. Interval coverage probability of level 95% for two deblurring problems with Gaussian noise level σ . Averaged on 20 test images.

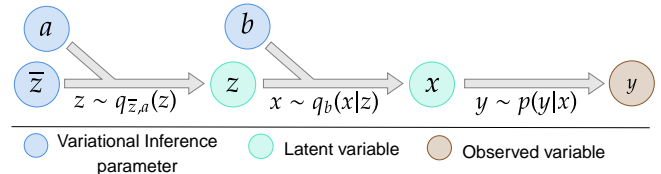


Figure 2. Generative model graph of our variational inference algorithm.

representation error (when the solution is not in the generator range). While the first two errors can reasonably be modelled by the latent posterior in VBLE, the representation error lies inherently in the image space, thus is hardly taken into account in the latent space. Therefore, we hypothesize that VBLE underestimates the uncertainties mainly because of this source of error. In Tab. 1, the second line corresponds to ICP results with a dataset that we called ManifoldCelebA. This dataset consists of CelebA images which have been encoded and decoded with the VAE, so that the representation error is null. ICPs for ManifoldCelebA are much closer to 0.95, validating our hypothesis.

4.4 Proposed joint latent and image posterior model

In the following, we propose a new method for image restoration, derived from VBLE, in which we model the inverse problem posterior jointly in the latent and image space in order to better model the representation error. For the sake of simplicity, we only consider one latent variable z , but the equation can easily be adapted for two latent variable CAEs by considering a concatenated variable $\psi = (z, h)$ and $p(\psi) = p(z|h)p(h)$.

We aim to estimate the joint latent and image inverse problem posterior $p_{X,Z|Y}(x, z|y)$ using variational inference. Note that for VBLE, the targeted distribution was the latent posterior $p_{Z|Y}(z|y)$. For that purpose, we consider the following parametric family, corresponding to the

representation of Fig. 2:

$$\begin{aligned}
E_{\bar{z},a,b} &= \{q_b(x|z)q_{\bar{z},a}(z)|\bar{z}, a \in \mathbb{R}^{C \times M \times N}, \\
& b \in \mathbb{R}^{C' \times M' \times N'} a, b > 0\} \\
\text{with } q_{\bar{z},a}(z) &= \prod_k \mathcal{U}(z_k; [\bar{z}_k - \frac{a_k}{2}, \bar{z}_k + \frac{a_k}{2}]). \\
q_b(x|z) &= \prod_k \mathcal{N}(D_\theta(z)_k, b_k^2 \sigma_\theta(z)_k^2)
\end{aligned}$$

with C' , M' and N' being the channel and spatial dimensions of the image space, $\sigma_\theta(z)$ being the deviation of the generative model $p_\theta(x|z) = \mathcal{N}(D_\theta(z), \Sigma_\theta(z)) := \text{diag}(\sigma_\theta(z)^2)$. This parametric distribution is composed of a latent term $q_{\bar{z},a}(z)$ and of an image term $q_b(x|z)$ which was designed to take into account the representation error. As in VBLE, the latent term is chosen to be uniform as it matches the CAE encoder distribution. The choice for $q_b(x|z)$ is motivated by the fact that $p_\theta(x|z)$ represents the likelihood of generating x given z . Hence, even if the representation error for an image x^* is nonzero (that is $D_\theta(z) \neq x^*$), x^* should nevertheless lie in a zone where $p_\theta(x|z)$ is high. Then, parameter b allows to better adapt the posterior model to the given inverse problem.

Then, variational inference parameters (\bar{z}, a, b) are optimized by minimizing $\text{KL}(q_b(x|z)q_{\bar{z},a}(z)||p_{X,Z|Y}(x, z|y))$, which amounts to maximizing the ELBO:

$$\begin{aligned}
\mathcal{L}(\bar{z}, a, b; y) &= \mathbb{E}_{q_b(x|z)q_{\bar{z},a}(z)} [\log p_{Y|X}(y|x) \\
& + \log p_\theta(x|z) + \log p_\theta(z) - \log q_b(x|z) - \log q_{\bar{z},a}(z)]
\end{aligned} \quad (15)$$

with $p_\theta(z)$ being the latent prior of the generative model, that is the hyperprior in the CAE case. Then, the $(x|z)$ terms represent a KL divergence between two Gaussian distributions and can be easily simplified, as well as $\log q_{\bar{z},a}(z)$ which is independent of z . Thus:

$$\begin{aligned}
\mathcal{L}(\bar{z}, a, b; y) &= \mathbb{E}_{q_b(x|z)q_{\bar{z},a}(z)} [\log p_{Y|X}(y|x) \\
& + \log p_\theta(z)] + \sum_k \log a_k + \sum_i \log b_i - \frac{1}{2} b_i^2.
\end{aligned} \quad (16)$$

With the reparameterization trick

$$\begin{aligned}
z &= \bar{z} + au, u \sim \mathcal{U}\left(\frac{-1}{2}, \frac{1}{2}\right) \\
x &= D_\theta(z) + b\sigma_\theta(z)\epsilon, \epsilon \sim \mathcal{N}(0, I),
\end{aligned} \quad (17)$$

eq. (16) can be optimized using gradient descent with a Monte Carlo approximation of the ELBO gradient as in [38, 5].

4.5 Learning the generator variance

The algorithm presented in the last section requires the following generative model: $p_\theta(x|z) =$

$\mathcal{N}(D_\theta(z), \text{diag}(\sigma_\theta(z)^2))$, thus the generator should estimate a pixelwise variance $\sigma_\theta(z)$. However, in classical VAE and CAE models, the decoder distribution is a Gaussian distribution $p_\theta(x|z) = \mathcal{N}(D_\theta(z), \gamma^2 I)$ with a fixed perpixel standard deviation γ responsible for the trade-off between the data fidelity and the latent constraint terms in the loss. This distribution is not appropriate in our case as the reconstruction error should be larger on high frequency areas than on large flat ones.

Some approaches learn more representative generator distributions [58, 19, 17]. Following [58], we add a second decoder predicting $\sigma_\theta(z)$, which has the same structure as the original decoder D_θ . We adopt a two stage training strategy as is typically done for training stability: first, the CAE is classically trained with a given γ trade-off parameter. Then, the second decoder is trained by minimizing the negative log-likelihood $\mathbb{E}_{z \sim q_\phi(z|x)} [-\log p_\theta(x|z)]$, the other CAE parts being fixed.

4.6 Calibration of VBLE predicted uncertainties

Our method yields valuable and informative uncertainties, as it will be shown in the experiments. However our variational posterior does not exactly match the true inverse problem posterior. To further improve the uncertainty prediction, we also consider the calibration strategy proposed in [54], which was shown to propose consistent error bounds for different posterior sampling methods. Specifically, this approach consists of learning, through a calibration subset, the quantiles of the true reconstruction error conditioned on an estimate of the posterior variance. Afterward, for a given pixel, the α -quantile of the true reconstruction error given the pixel posterior variance represents an error bound of level α . We refer to [54] for further details.

5 Experimental setting

In the experiments, we address the problem of satellite panchromatic image restoration, that is deblurring and denoising of one spectral band typically spanning wavelengths from 450nm to 850nm. In addition, we study the joint problem of restoration and super-resolution as satellite images are more and more super-resolved. For both problems, we chose the operating point of Pléiades satellites, as it constitutes a reference for very high resolution optical satellite imaging in Europe, for which we know well the degradation model. In this section, we present the considered inverse problems. Then, data collection and processing are detailed. Finally, the experiment setup is provided, including the evaluation metrics, the considered baselines, and the training details for the proposed methods.

5.1 Forward models and considered inverse problems

Deep regularization methods are model-based, thus require the log-likelihood of the forward model $p_{Y|X}(y|x)$ as it is used during the restoration process. The blurring process can hardly be exactly modelled, as the observed landscape, as well as the blur kernel, are continuous. Hence, we consider the forward model to be:

$$y = \mathcal{D}(h * x_{target}) + w \quad (18)$$

where y is the measure, x_{target} the target image at the target resolution, h the blur kernel *sampled at the target resolution*, \mathcal{D} corresponds to a downsampling operator, and w is the approximated Poisson-Gaussian noise of variance $\sigma_w^2(x_{target}) = \sigma_0^2 + K(\mathcal{D}(h * x_{target}))$. In the experiments, we consider two inverse problems. The first one, called IR, consists of joint denoising and deblurring. In this case, $\mathcal{D} = I$. The second one, called IR+SISR, consists of joint denoising, deblurring, and super-resolution by a factor of 2.

5.2 Detailed data processing

	#imgs	Source resolution	#bits	Covered area (km^2)	Size (\downarrow 50cm)	Size (\downarrow 25cm)
Pélican	95	10cm	12	18.45	128MB	512MB
PCRS	510	5cm	12	537.18	4.3GB	17.2GB

Table 2. PCRS (IGN) and Pélican (CNES) databases characteristics. \downarrow 50cm (resp. 25cm) corresponds to the information of the database downsampled at a resolution of 50cm (resp. 25cm).

In this paper, we use simulated data to train SatDPIR, VBLE-xz, and the deep learning baselines. For the image restoration experiments, both simulated and real satellite data are used. The simulated images are produced using two databases: PCRS, provided by IGN [1], and Pélican, provided by CNES. Both datasets are composed of airplane images acquired at a very high resolution, that is 5cm for PCRS and 10cm for Pélican. Target and degraded satellite images are then obtained by downsampling them. The characteristics of each database are provided in Tab. 2.

5.2.1 Simulated satellite images

To train DR methods SatDPIR and VBLE-xz, as well as direct inversion baselines, target satellite images are required. Simulated degraded images are also needed to evaluate the performance of the different methods, as well as to train direct inversion baselines. To create target images, very high resolution PCRS and Pélican images are downsampled at the target resolution, that is 50cm for IR and 25cm for IR+SISR, after applying an anti-aliasing filter. By downsampling these images by a sufficient factor, we consider the initial airplane blur to be negligible, thus creating

”ideal” noise and blur free satellite images. To create the degraded images, the blur kernel, modelling the satellite point spread function (PSF), is applied to Pélican and PCRS aerial images, before downsampling them at the satellite resolution, that is 50cm in all simulated experiments, adding the instrument noise and quantizing them on 12 bits. Note that in this simulation pipeline, degraded images do not exactly follow our forward model of eq. (18), because of PSF subsampling and image quantization, which is coherent with a realistic context where the forward model is always imperfect.

5.2.2 Real satellite images

Experiments on real data are performed using Pléiades 12 bits images. These images are acquired at a resolution of 70cm (but commercialized at 50cm after an upsampling that enhances the image robustness to post-processing). Note that, unlike the simulated images, the real images have been compressed at 2.86bits/pixel [40] and decompressed. For these images, we choose to neglect the compression when modelling the data log-likelihood, which is required for SatDPIR and VBLE computations. This is relevant as the compression rates for satellite images are very high. Therefore, we consider the impact of compression-decompression as a source of error, among others, in the real image model.

5.2.3 Train and test datasets

For the simulated test set, a subset of 30 images from the Pélican dataset is chosen, representing various landscapes such as desert, industrial, and urban areas. Degraded images are simulated at a resolution of 50cm, and are sized 820×820 . We denote this test set as TEST30_SIMU. All PCRS images and the other Pélican images are used in the training and validation set. For some experiments, only a subset of TEST30_SIMU is used, denoted TEST14_SIMU. It contains 14 images, center cropped to sizes 512×512 for IR and 256×256 for IR+SISR experiments. To test the algorithms on real Pléiades images, three landscapes are chosen: ATACAMA, DENVER, and SHANGHAI to form TEST30_REAL dataset. It contains 10 images of each landscape, each image being 820×820 at a resolution of 70cm.

5.3 Experiment setup

5.3.1 General training settings

The neural networks used in VBLE-xz and SatDPIR are trained at each used target resolution, that is 50cm and 25cm for the IR and IR+SISR experiments on simulated data, 70cm and 35cm for the IR and IR+SISR experiments on real data.

5.3.2 Compressive autoencoder details

For VBLE-xz, we choose CAE architecture from [52]. It is a CAE with hyperprior, with a simple convolutional encoder and decoder. We employ models from compressAI library [8] that have been pretrained at different bitrates and we finetune them on satellite images at a given target resolution for 150k iterations. Afterward, we train the variance decoder as described in Sec. 4.5 using satellite images during 100k iterations.

5.3.3 Denoiser details

DRUNet denoiser [76] is used for SatDPIR. DRUNet is a state-of-the-art deep convolutional denoiser specifically tailored for image restoration. We employ a pretrained model from [76] that we finetune at a given target resolution on satellite images, during 500k iterations.

	SRResNet	RDN	DRUNet	CAE
#params	1.3M	22M	32M	25M

Table 3. Number of parameters of the different networks used in the experiments

5.3.4 Baselines

SatDPIR and VBLE-xz are compared to several baselines to assess their performance. First, for uncertainty quantification evaluation, we compare VBLE-xz to two posterior sampling methods: PnP-ULA [41], a state-of-the-art MCMC posterior sampling method that employs a denoiser as prior; and VBLE [5], which is a natural baseline for VBLE-xz. For PnP-ULA, we choose the DRUNet denoiser, that is the denoiser used for SatDPIR, and for VBLE we choose the same CAE as for VBLE-xz. Then, to assess the performance of VBLE-xz and SatDPIR without uncertainty quantification, we consider the following baselines. Bay+IF [40] is a classical approach that is currently being used in the Pléiades ground segment. It is composed of two steps: denoising is performed using NL-Bayes [42], then inverse filtering is used for deblurring. For super-resolution experiments, Bay+IF images are upsampled using bicubic upsampling. Then, we consider two direct inversion baselines, SRResNet and RDN. SRResNet [43] is a light convolutional neural network composed of a succession of residual blocks. This network has already been adapted for satellite image restoration and SISR [81, 12]. RDN [79] is a deeper and wider convolutional network, which uses residual blocks with dense connections. For both networks, we adopt the loss proposed in [12]: $\mathcal{L}(x, \hat{x}) = \alpha \text{SmoothL1}(x, \hat{x}) + \beta \text{DISTS}(x, \hat{x})$ where SmoothL1 is a smooth version of the L1 distance, and DISTS [16] is a perceptual loss. SRResNet and RDN are trained from scratch

during 200k iterations, corresponding to convergence. In Tab. 3, the number of parameters of every neural network used in the experiments is provided.

5.3.5 Restoration hyperparameters

For several methods, restoration hyperparameters are tuned by grid search on a validation set of 3 Pélican images for each inverse problem. For SatDPIR, the regularization parameter λ is tuned accordingly. For VBLE-xz (and VBLE), we also introduce a regularization parameter λ in eq. (15) as follows:

$$\arg \max_{\bar{z}, a, b} \mathbb{E}_{q_b(x|z)q_{z,a}(z)} [\log p_{Y|X}(y|x) + \lambda (\log p_\theta(x|z) + \log p_\theta(z) - \log q_b(x|z) - \log q_{z,a}(z))], \quad (19)$$

$\lambda = 1$ corresponding to the Bayesian framework. We choose $\lambda = 0.6$ in all VBLE and VBLE-xz experiments because it yields the best trade-off between performance and uncertainties quality, as will be shown in Fig. 12 of the ablation study. For PnP-ULA, the regularization parameter, the denoiser noise level, and the chain step size are tuned accordingly, while 10^5 iterations are performed for each restoration.

5.3.6 Evaluation metrics

To evaluate the image restoration performance when ground truth is available, three metrics have been used: the Peak Signal-to-Noise Ratio (PSNR), the Structural SIMilarity (SSIM) [67], and the Learned Perceptual Image Patch Similarity (LPIPS) [78]. The PSNR represents the accuracy between the restored and target images, while the SSIM and LPIPS are respectively classical and deep learning perceptual metrics. For no reference image quality assessment, we employ the Blind Referenceless Image Spatial Quality Evaluator (BRISQUE) [53]. BRISQUE provides a score between 0 and 100, based on the deviation of the statistic of some local features with respect to natural images, the lower being the better. Finally, to evaluate quantitatively the predicted uncertainty quantification of posterior sampling methods, we compute Interval Coverage Probability (ICP) of level α . It represents the proportion of the perpixel true error that is contained in the perpixel predicted error quantiles of level α . Thus, the closer to α , the better.

6 Experimental results

6.1 Uncertainty quantification results on simulated data

In this section, we assess the performance and interest of the posterior samples and uncertainty quantification provided by VBLE-xz compared to VBLE [5] and PnP-ULA

IR	PnP-ULA	VBLE	VBLE-xz not calibrated	VBLE-xz
PSNR \uparrow	48.63	48.40	48.35	48.35
ICP 90%	0.92	0.79	0.83	0.91
Time	2h10m	17.7sec	27.3sec	27.3sec
IR+SISR	PnP-ULA	VBLE	VBLE-xz not calibrated	VBLE-xz
PSNR \uparrow	35.86	37.45	37.38	37.38
ICP 90%	0.94	0.67	0.73	0.91
Time	2h21m	19.5sec	29.4sec	29.4sec

Table 4. Comparison between posterior sampling methods on TEST14_SIMU for IR and IR+SISR. Time denotes the time required to restore and then draw 100 posterior samples for each method given a 512^2 image for IR and 256^2 for IR+SISR. Times are obtained with a Nvidia Quadro RTX8000 GPU.

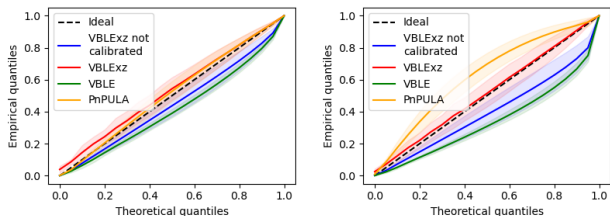


Figure 3. Interval coverage probabilities for the IR problem (left) and IR+SISR problem (right). Each point of a curve of abscissa α provides the ICP of level α averaged on the test dataset. Colored areas correspond to deviations. The closer to the identity, the better.

[41]. We perform these experiments on TEST14_SIMU. In Sec. 6.1 we report the PSNR, the 90% ICP (defined in Sec. 5.3.6) as well as the computation time required to restore an image and draw 100 posterior samples, with best values in bold font. First, a key aspect of VBLE-xz is its computation time to draw 100 posterior samples. Indeed, it is by several orders of magnitude faster than PnP-ULA, making this method scalable for satellite image restoration, unlike PnP-ULA. In terms of PSNR, PnP-ULA exhibits consistent results for image restoration, but it is outperformed by VBLE and VBLE-xz in super-resolution. In Fig. 3, coverage probabilities, that is ICP of level α for α varying from 0 to 1, are provided for each method on IR and IR+SISR. The 90% ICP of Sec. 6.1 corresponds to the point with abscissa 0.9. First, we observe that VBLE-xz without calibration obtains better 90% ICPs than VBLE, showing the interest of modelling the reconstruction error. While empirical coverage probabilities show that VBLE-xz without calibration still underestimates the uncertainty, the calibration procedure solves the problem, enabling our method to be competitive with PnP-ULA ICPs for IR, and clearly outperforming it for IR+SISR.

Additionally, the interest of VBLE-xz over VBLE is visually assessed in Fig. 4. This figure shows the true per-pixel error, as well as the 90% perpixel predicted error quan-

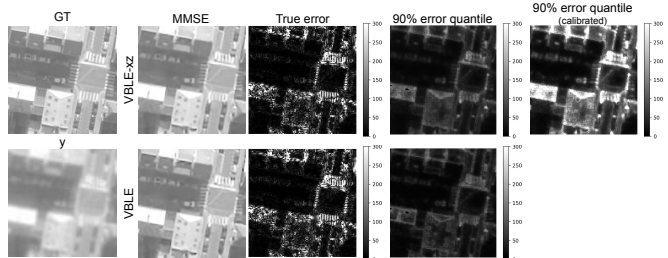


Figure 4. Difference between VBLE and VBLE-xz posterior sampling ability. The true error is $e = |GT - MMSE|$ while the error quantile map represents the perpixel 90% quantile of the predicted error. The calibrated version refers to the improvement proposed in Sec. 4.6. ©CNES 2024

tiles for VBLE, VBLE-xz without calibration, and VBLE-xz with calibration. VBLE-xz, even without calibration, possesses more realistic quantiles, as the quantile map has higher values and exhibits higher uncertainties on some uniform zones as roofs, while VBLE seems to concentrate the uncertainty on the edges. With calibration, VBLE-xz is able to provide very accurate uncertainty quantification, as the quantile map resembles the true perpixel error. Lastly, a thorough visual study of each method’s posterior sampling ability is provided in Fig. 5. This figure shows the MMSE estimate of each method obtained by averaging 100 posterior samples, as well as two posterior samples, the true error, and the 90% error quantile map. PnP-ULA posterior samples are very noisy for IR+SISR, making them hardly usable in practice. VBLE samples are visually better than those of PnP-ULA, but some details are unrealistic. In particular, in the shadow, the cars are sometimes distorted. VBLE-xz samples exhibit a little bit of noise as some uncorrelated noise is added in the image space, but this does not affect the image interpretation and VBLE-xz gets more realistic samples than VBLE. At last, the 90% error quantiles of VBLE-xz are consistent with the true error.

Hence, VBLE-xz provides better posterior samples and uncertainties than VBLE, validating the proposed joint latent and image posterior modelling. Furthermore, VBLE-xz outperforms PnP-ULA in terms of sampling ability, and computation speed. In particular, its low computation time for a posterior sampling method makes it scalable to restore real satellite images.

6.2 Point estimation results on simulated data

In this section, we present the results of the different methods on the TEST30_SIMU dataset. Quantitative metrics are presented in Tab. 5 while Fig. 6 contains visual results. Table 5 contains results for the image restoration problem, with (IR+SISR) and without super-resolution (IR). The results have been separated for each type of landscape, enabling a thorough comparison between the methods. First,

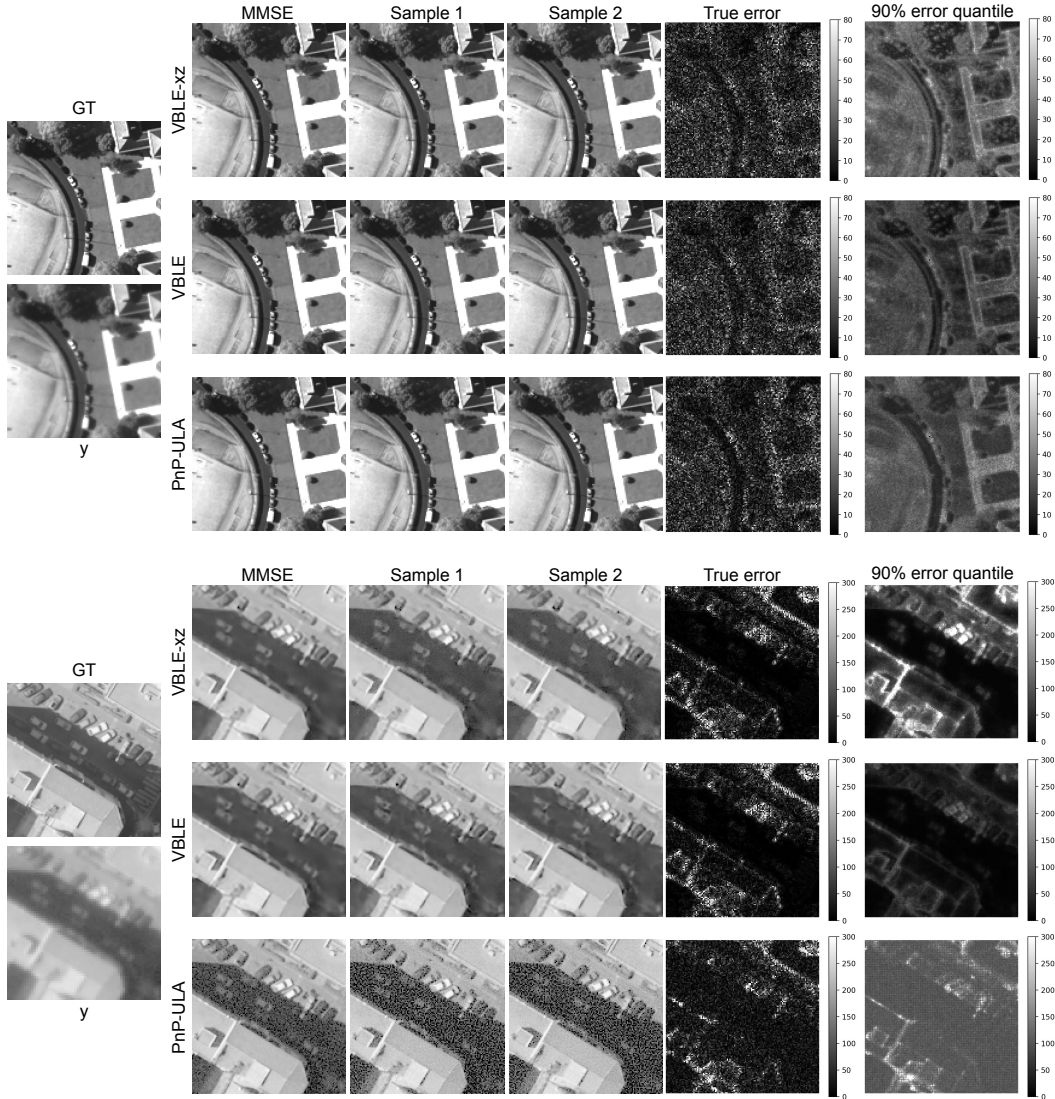


Figure 5. Posterior sampling ability of various methods on TEST14_SIMU. Top: IR problem, Bottom: IR+SISR problem. MMSE estimates are averaged on 100 posterior samples. The true error is $e = |GT - MMSE|$ while the error quantile map represents the perpixel 90% quantile of the predicted error. VBLE-xz quantiles are calibrated, as proposed in Sec. 4.6. ©CNES 2024

the Bay+IF method is by far outperformed by all deep learning methods. Then, SatDPIR outperforms direct inversion methods RDN and SRResNet in terms of PSNR and SSIM, while being slightly below them in terms of LPIPS. This is expected because inversion methods are partly trained with a perceptual loss, DISTs, which is similar to LPIPS, whereas DR methods only consider the pixelwise likelihood. This can be visually illustrated in Fig. 6. Indeed, direct inversion methods exhibit sharper results with more high frequency details, which is favorable to a low LPIPS. However, the added high frequencies are not necessarily correct. Moreover, they show non desirable oscillating deconvolution artifacts, for example in the 5th image of Fig. 6.

Compared to the other methods, VBLE-xz exhibits slightly poorer metrics than SatDPIR, but remains competitive with the baselines in terms of PSNR and LPIPS. Visually, VBLE-xz is particularly interesting as its MMSE result is a bit smoother than the other method, but exhibits very few artefacts, compared to direct inversion methods, and also to SatDPIR, which invents some lines in the 3rd image of Fig. 6.

The computation time needed to restore one image is also provided in Tab. 5, except for Bay+IF, which runs on CPU. First, the computation time is much higher when super-resolution is performed, as it is necessary to divide images into patches for all methods except SRResNet. Then, the computation time of SatDPIR without super-

		IR						IR+SISR				
		Degraded image y	Bay+IF	RDN	SRResNet	SatDPIR	VBLE-xz	Bay+IF (+bicubic)	RDN	SRResNet	SatDPIR	VBLE-xz
DENSE URBAN	PSNR \uparrow	30.74	38.12	47.00	47.86	47.89	47.42	31.14	35.27	34.89	35.61	35.25
	SSIM \uparrow	0.9083	0.9841	0.9964	0.9964	0.9964	0.9958	0.8929	0.9453	0.9415	0.9491	0.9447
	LPIPS \downarrow	0.1477	0.0233	0.0065	0.0067	0.0063	0.0104	0.2366	0.1028	0.1219	0.1450	0.1618
LIGHT URBAN	PSNR \uparrow	31.16	38.59	47.50	47.98	48.09	47.61	31.49	36.00	35.52	36.42	35.83
	SSIM \uparrow	0.9155	0.9849	0.9960	0.9958	0.9960	0.9954	0.9037	0.9512	0.9474	0.9554	0.9506
	LPIPS \downarrow	0.1436	0.0280	0.0089	0.0095	0.0085	0.0153	0.2416	0.1067	0.1280	0.1478	0.1669
RURAL	PSNR \uparrow	36.30	42.60	48.01	48.04	48.20	47.70	35.27	37.45	37.28	38.05	37.47
	SSIM \uparrow	0.9346	0.9830	0.9918	0.9917	0.9919	0.9907	0.8972	0.9232	0.9229	0.9319	0.9211
	LPIPS \downarrow	0.1722	0.1045	0.0263	0.0273	0.0255	0.0484	0.3060	0.1729	0.1942	0.2338	0.2831
DESERT	PSNR \uparrow	44.06	47.04	48.49	48.57	48.74	47.89	40.01	39.65	39.87	40.60	40.05
	SSIM \uparrow	0.9703	0.9830	0.9876	0.9875	0.9878	0.9850	0.9154	0.9150	0.9126	0.9256	0.9128
	LPIPS \downarrow	0.2058	0.1045	0.0511	0.0513	0.0514	0.1181	0.4052	0.2263	0.2632	0.3212	0.3764
WATER	PSNR \uparrow	36.54	44.01	<u>52.84</u>	51.86	53.07	52.82	36.09	40.01	39.38	40.44	<u>40.12</u>
	SSIM \uparrow	0.9705	0.9945	0.9984	0.9977	0.9983	0.9982	0.9650	0.9810	0.9785	0.9829	0.9810
	LPIPS \downarrow	0.0877	0.0302	0.0101	0.0178	0.0091	0.0193	0.1075	0.0658	0.1133	0.0758	0.0801
PORT	PSNR \uparrow	30.28	37.91	46.96	<u>48.03</u>	48.20	47.86	29.38	<u>32.73</u>	32.31	32.97	32.47
	SSIM \uparrow	0.9401	0.9897	0.9974	0.9972	0.9975	0.9971	0.9152	0.9517	0.9474	0.9549	0.9496
	LPIPS \downarrow	0.1065	0.0313	0.0108	0.0129	0.0089	0.0225	0.1785	0.0945	0.1263	0.1175	0.1345
FOREST	PSNR \uparrow	31.53	38.87	<u>47.28</u>	<u>47.30</u>	47.39	47.12	32.00	34.72	34.51	35.10	34.93
	SSIM \uparrow	0.9184	0.9862	0.9965	0.9964	0.9965	0.9961	0.9048	0.9429	0.9410	0.9485	0.9450
	LPIPS \downarrow	0.1689	0.0334	0.0115	0.0124	0.0109	0.0185	0.2567	0.1240	0.1472	0.1938	0.2248
INDUSTRIAL	PSNR \uparrow	35.52	42.45	48.59	<u>48.99</u>	49.29	48.73	34.89	38.17	37.69	38.65	<u>38.33</u>
	SSIM \uparrow	0.9358	0.9863	0.9943	0.9940	0.9944	0.9935	0.9143	0.9481	0.9447	0.9543	0.9469
	LPIPS \downarrow	0.1352	0.0398	0.0169	0.0179	0.0160	0.0333	0.2573	0.1339	0.1542	0.1693	0.1894
TOTAL	PSNR \uparrow	33.55	40.56	48.08	48.44	48.66	48.19	33.22	36.66	36.28	37.18	36.63
	SSIM \uparrow	0.9289	0.9859	0.9951	0.9949	0.9952	0.9944	0.9088	0.9460	0.9430	0.9513	0.9452
	LPIPS \downarrow	0.1437	0.0369	0.0145	0.0157	0.0138	0.0275	0.2463	0.1228	0.1466	0.1658	0.1897
Computation time		x	x	4.2s	0.4s	3.7s	62.3s	x	5.0s	0.9s	1min08s	3min20s

Table 5. Quantitative results on TEST30_SIMU for IR and IR+SISR problems. Best results are in bold, while second best results are underlined. Computation times are obtained using a Nvidia Quadro RTX8000 GPU.

resolution is very fast, and even faster than RDN. When super-resolution is performed, direct inversion methods are faster, even if DR methods’ computation time remains scalable. It is worth noting that SatDPIR computation time has been greatly improved compared to DPIR by our proposed adaptation in Sec. 3, as will be detailed in Tab. 8 of the ablation study. Concerning VBLE-xz, its computation time is slightly above the others. This is expected as VBLE-xz enables posterior sampling. Yet, it remarkably stays computationally scalable. Besides, recall that this is rarely the case with other posterior sampling methods as VBLE-xz is much faster than PnP-ULA as depicted in Sec. 6.1 of the previous section.

Therefore, SatDPIR provides excellent results as it reaches direct inversion methods performances, and even outperforms them in terms of PSNR, even though SatDPIR is a plug-and-play method that has not been trained to solve a specific inverse problem. It is also very fast for IR, a bit slower than RDN and SRResNet for IR+SISR but stays computationally efficient. Furthermore, VBLE-xz, whose posterior sampling ability has been demonstrated in the previous section, exhibits very consistent results compared to the baselines, which only compute a point estimate. Its computation time is slightly bigger, however stays remarkably low for a posterior sampling method.

6.3 Results on real satellite images

In this section, we present the results of the different methods on TEST30_REAL. As we do not have access to any ground truth, the analysis will be essentially based on visual results. Additionally, we provide BRISQUE scores in Sec. 6.3, though this metric exhibits high variance and might not be fully adapted to satellite images. CI refers to the Commercialized (Pléiade) Image. Direct inversion methods exhibit the best BRISQUE scores for the IR+SISR problem, which can be explained by their sharp results involving ”typical” high frequencies that are not necessarily accurate. However, in IR, VBLE-xz is competitive with the direct inversion baselines.

Pb.	y	CI	RDN	SRResNet	DPIR	VBLE-xz
IR	ATAC.	41.20	51.09	24.85	50.11	46.96
	DENV.	27.48	27.88	30.34	23.89	24.74
	SHAN.	32.43	31.93	27.21	27.90	31.40
	TOTAL	33.70	36.97	24.13	33.97	34.37
IR+SISR	ATAC.	x	56.30	19.13	30.51	54.57
	DENV.	x	40.15	5.42	14.39	36.47
	SHAN.	x	39.31	5.79	12.64	42.64
	TOTAL	x	45.25	10.11	19.18	44.56

Table 6. BRISQUE \downarrow scores on TEST30_REAL. ATAC., DENV. and SHAN. stand resp. for Atacama, Denver and Shanghai landscapes. CI stands for the commercialized image.

Visual results are given in Fig. 7 and in Fig. 8. In Fig. 7, the measure contains some compression artefacts which are amplified by in the commercialized image (CI). All deep

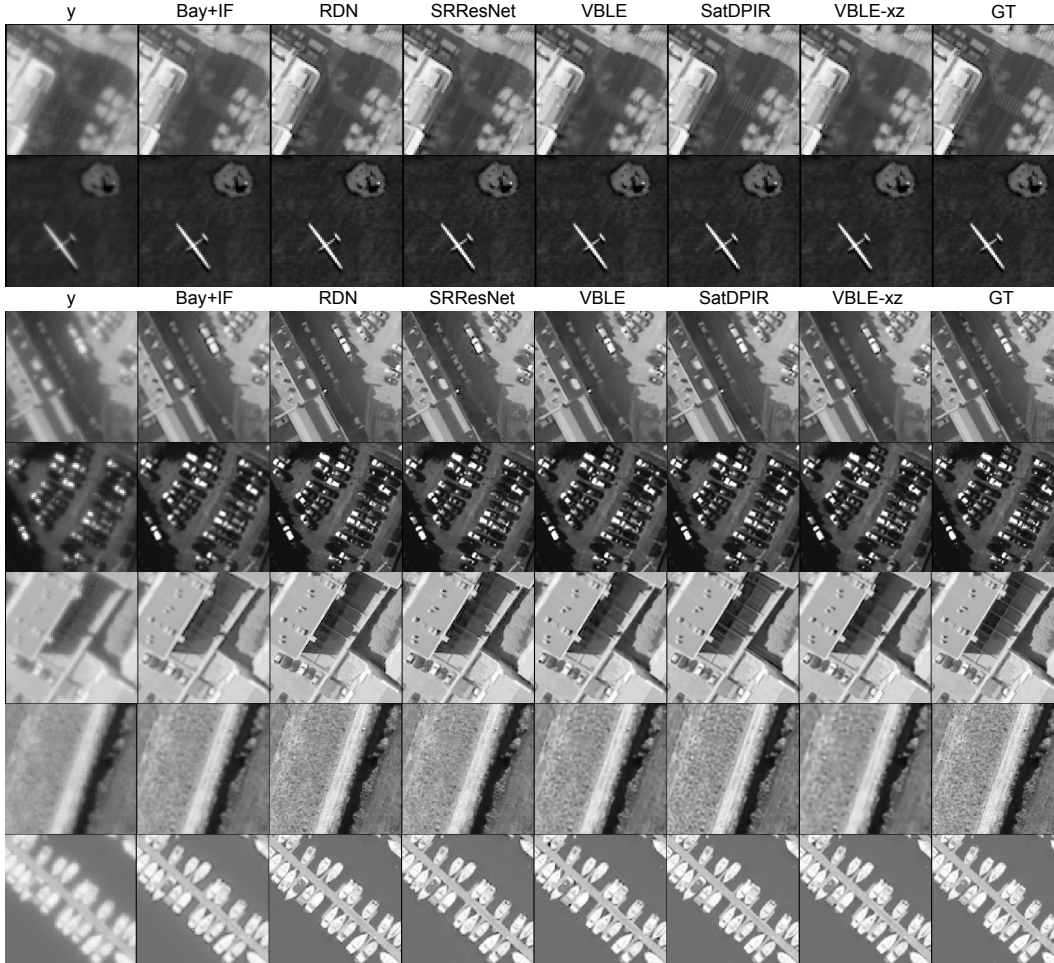


Figure 6. Qualitative results of SatDPIR, VBLE-xz and the baselines on TEST30_SIMU. The first two lines correspond to the IR problem, the others correspond to IR+SISR. ©CNES 2024

learning methods perform better than CI for removing these artefacts. However, for RDN and SRResNet, some of the artefacts still slightly remain, while DR methods manage to remove them entirely. Indeed, direct inversion methods yield sharper results but deconvolve details that are not present in the true image.

Figure 8 shows the results of image restoration with super-resolution for all methods. For VBLE-xz, the MMSE estimate, as well as two posterior samples and the predicted 90% perpixel quantiles are provided. The zoomed commercialized image is very blurry, direct inversion methods yield sharp results, but with some artefacts, while DR methods provide smoother results. SatDPIR provides excellent results, however, it sometimes yields lines that do not exist. VBLE-xz provides very consistent results, its MMSE estimate is rather smooth, but the samples are sharper and contain valuable information. For instance, in the zoomed area, two forms are proposed for the linear and both seem plausible. Besides, the 90% quantile map provides a meaningful

way to localize unsure areas.

6.4 Robustness evaluation

In this section, we evaluate the robustness of the different methods to resolution and model changes using TEST30_SIMU.

6.4.1 Resolution robustness

Direct inversion models are problem specific, therefore need to be retrained or fine-tuned for each resolution and each inverse problem. For DR methods VBLE-xz and SatDPIR, the models can be used to restore several inverse problems, yet, it should *a priori* be retrained for each resolution. In the resolution experiments, we evaluate the robustness on IR and IR+SISR problems. For IR, we use the DR models trained on 25cm target images and evaluate them on 50cm images. For direct inversion methods, RDN and SRResNet are trained to deblur 25cm images and are evalu-

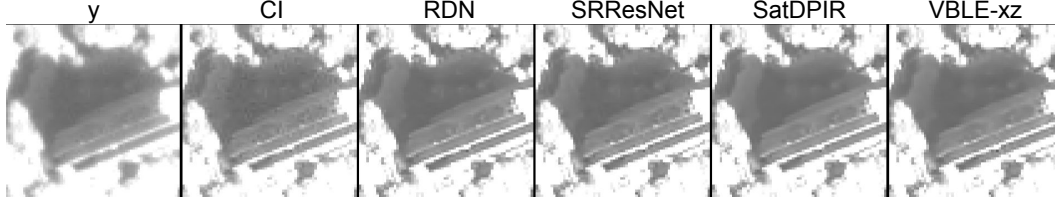


Figure 7. Handling of compression artefacts for each method. Restoration results of several methods on a real DENVER satellite image of TEST30_REAL, for the IR problem. CI stands for the commercialized image. ©CNES 2024

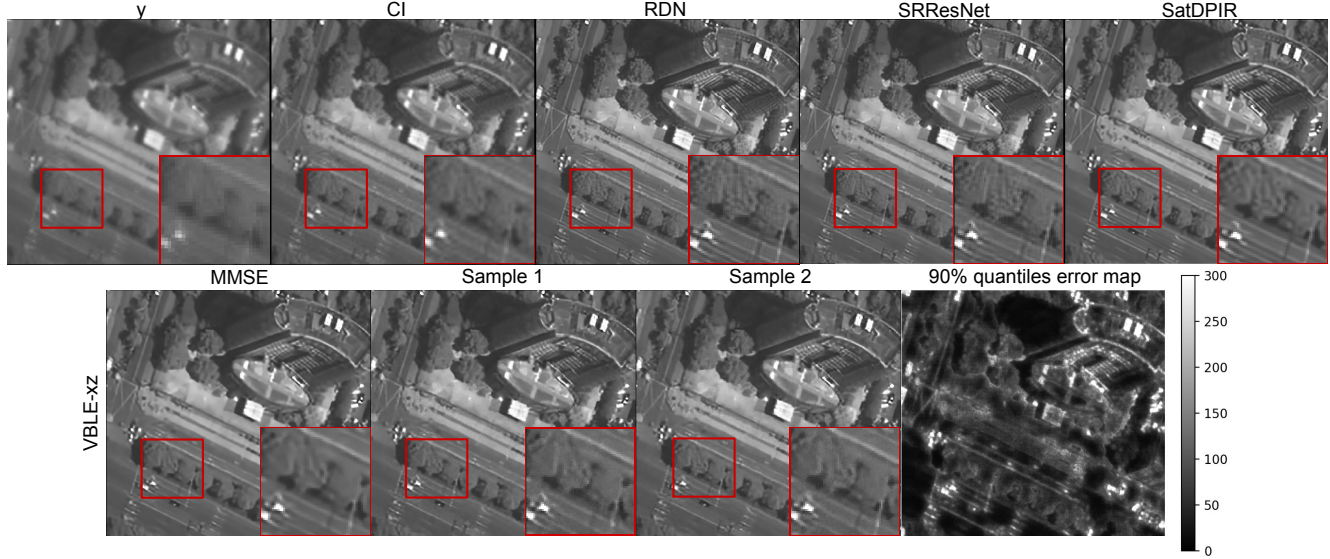


Figure 8. Results for several methods on a real DENVER satellite image of TEST30_REAL, for IR+SISR problem. CI stands for commercialized image. ©CNES 2024

ated on 50cm images. For IR+SISR, we use the DR models trained at 50cm and evaluate them on 25cm images. Quantitative results are provided in Tab. 7. Surprisingly, for all methods, the performance is not significantly affected by the resolution change. This could be explained by the fact that some invariance to resolution exists in several satellite landscapes, for instance in textured areas. It is however not the case for some small or high frequency structures, such as cars or pedestrian crossings. In Fig. 9, which provides the restoration of a pedestrian crossing for each method at the two resolutions, the crossing is restored worse with the model trained at the wrong resolution. This is particularly visible for SatDPIR as it restores particularly well the crossing at the right resolution.

6.4.2 Robustness to model changes

Then, we evaluate the robustness of the different methods to changes in the forward model. We choose, for simplicity, to induce slight changes in the PSF, parameterized by the Modulated Fourier Function (MTF), that is the Fourier transform of the PSF, evaluated at $f_e/2$. The Pléiades MTF at $f_e/2$ is 0.15. We compute image restoration results for

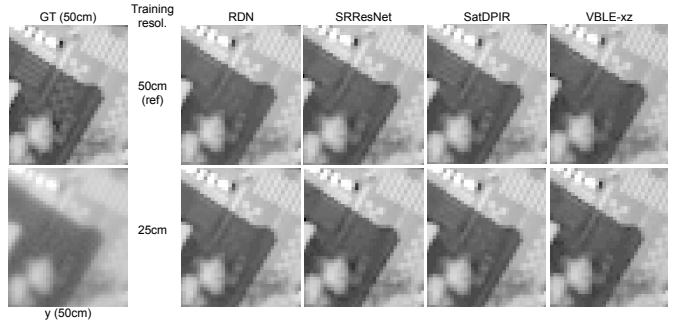


Figure 9. Restored image from TEST30_SIMU by several methods for the IR problem, using a network trained at the right resolution (first row), and a network trained at the wrong resolution (second row). ©CNES 2024

MTF values of 0.13 and 0.12 at $f_e/2$. These values are representative of the evolution of the instrument PSF in orbit. As direct inversion methods are trained for a specific PSF with $MTF = 0.15$, they should not be very robust to these changes. For DR methods, if the change of PSF is taken into account in the forward model during the restoration, the

	Training Resol.	IR			Training Resol.	IR+SISR		
		PSNR \uparrow	SSIM \uparrow	LPIPS \downarrow		PSNR \uparrow	SSIM \uparrow	LPIPS \downarrow
RDN	50 (ref)	48.08	0.9951	0.0145	25 (ref)	x	x	x
	25	48.00	0.9951	0.0144	50	x	x	x
SRResNet	50 (ref)	48.44	0.9949	0.0157	25 (ref)	x	x	x
	25	48.16	0.9948	0.0165	50	x	x	x
DPIR	50 (ref)	48.66	0.9952	0.0138	25 (ref)	37.18	0.9513	0.1658
	25	48.78	0.9953	0.0142	50	37.31	0.9542	0.1527
VBLE-xz	50 (ref)	48.19	0.9944	0.0275	25 (ref)	36.63	0.9452	0.1897
	25	48.10	0.9946	0.0242	50	36.56	0.9446	0.1917

Table 7. Quantitative results for resolution robustness experiments on TEST30_SIMU. For each method and each problem, the first line corresponds to the results using the network trained at the right resolution, while the second line denotes the results using the network trained at the wrong resolution.

performance should not be affected. A visual illustration is given in Fig. 11, while quantitative results are provided in Fig. 10.

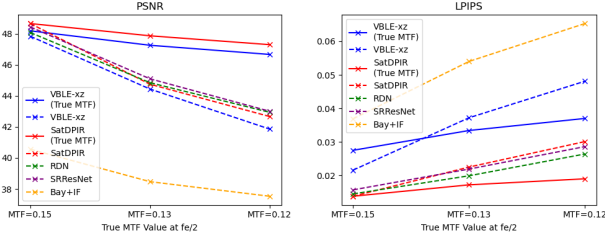


Figure 10. PSNR and LPIPS of several methods with changes in the forward model. Dashed lines denote the results without modelling the change. For DR methods SatDPIR and VBLE, continuous lines denote the results when the change is modelled in the forward model during restoration. $MTF=0.15$ at $f_e/2$ is the original value of the MTF in the experiments.

Dashed lines in the figure represent the performance of the methods when the wrong PSF, with $MTF=0.15$, is used for image restoration. Continuous lines for DR methods represent the performance when the PSF change is integrated into the forward model. When the wrong PSF is used for DR methods, the performance decay is at the same rate as RDN and SRResNet methods. Yet, when the PSF change is integrated in the forward model, the performance is not affected, showing that DR methods can be used with different PSFs without any retraining, as long as the forward model is correctly specified. This can be crucial in practice as the PSF of a satellite evolves with time, mainly due to focus changes. Conversely, direct inversion networks should be retrained each time the PSF is significantly modified.

Therefore, SatDPIR and VBLE-xz are robust to resolution changes and to changes in the forward model. Additionally, they also work very well on real data, as shown in the previous section. These data contain new types of landscapes that have not been seen during training, i.e. clouds and Atacama desert, and additional model errors induced by compression and satellite off-pointing. This shows that the methods are robust to a wide range of problems and can

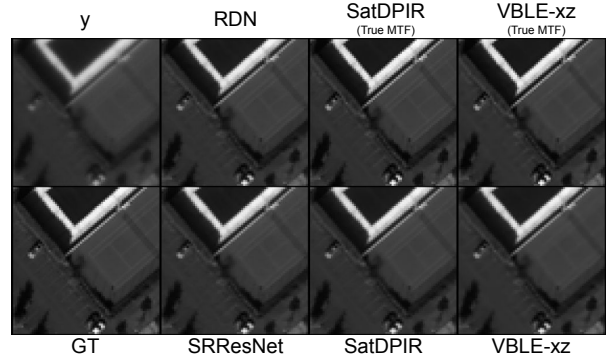


Figure 11. Restored image from TEST30_SIMU by several methods for the IR problem with changes in the degradation model ($MTF=0.12$ at $f_e/2$). This forward model change is not modelled, except for DR methods when *True MTF* is mentioned. ©CNES 2024

be used in practice in real satellite processing chains.

6.5 Ablation study

		DPIR	SatDPIR
IR	PSNR \uparrow	48.70	48.66
	LPIPS \downarrow	0.0139	0.0138
	Time	4.4s	3.8s
IR+SISR	PSNR \uparrow	37.19	37.18
	LPIPS \downarrow	0.1656	0.1658
	Time	18min09s	1min08s

Table 8. Comparison of DPIR and our proposed method SatDPIR. Results on TEST30_SIMU.

Table 8 highlights the interest of our proposed method, SatDPIR, compared to DPIR. SatDPIR has almost exactly the same metrics as DPIR, thus the solutions found by SatDPIR and DPIR are very close. Yet, SatDPIR is much faster especially when super-resolution is performed jointly to restoration. Indeed, for this problem, the computation of the data-fidelity proximal operator is very slow and the proposed accelerated framework enables to get results 20 times faster than DPIR.

Figure 12 shows diverse metrics for VBLE-xz for different values of λ regularization parameter. $\lambda = 1$ corresponds

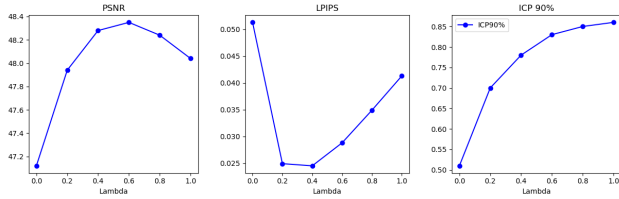


Figure 12. PSNR, LPIPS and 90% ICP of VBLE-xz (not calibrated) on TEST14_SIMU for the IR problem, for varying regularization parameter λ .

to the exact Bayesian framework. While the best PSNR and LPIPS are reached around $\lambda = 0.4$, the quality of the predicted (uncalibrated) ICPs strongly decreases for $\lambda < 0.6$. Hence, we have chosen $\lambda = 0.6$ for all the experiments, as it seems a good trade-off between the different metrics.

7 Conclusion

In this paper, we have introduced the VBLE-xz method for satellite image restoration, which estimates the inverse problem posterior using variational inference by capturing the uncertainty jointly in the latent and image space of a variational compressive autoencoder. We also proposed SatDPIR, which accelerates the original plug-and-play framework which, in the case of Poisson-Gaussian noise, requires an inner iteration process.

The conducted experiments demonstrate the interest of VBLE-xz as a scalable posterior sampling method for satellite image restoration, as it outperforms the state-of-the-art PnP-ULA method both in terms of performance and posterior samples realism while being by several orders of magnitude faster. Furthermore, the results of VBLE-xz and SatDPIR visually exhibit very few artefacts compared to state-of-the-art direct inversion methods, which is crucial for current satellite super-resolution chains. Quantitatively, VBLE-xz remains competitive with these baselines for point estimation results, and SatDPIR outperforms them in terms of PSNR and SSIM, excelling in deconvolving small details. This makes SatDPIR a very interesting alternative to direct inversion methods if only point estimation is required.

Future works will be dedicated to improving and extending the method, for instance by considering variable bitrate and fixed-quality CAEs [32], that would enable a local tuning of the regularization and should improve the results when the image contains both high-frequency and smooth areas. Another interesting perspective will be to demonstrate the interest in the generated uncertainties for real remote sensing use cases such as change detection or land-cover mapping.

Acknowledgments

This work was partly supported by CNES under project name DEEPREG, and ANITI under grant agreement ANR-19-PI3A-0004.

References

- [1] Institut national de l’information géographique et forestière (IGN). <https://geoservices.ign.fr/pcrs>.
- [2] J. Ballé, V. Laparra, and E. P. Simoncelli. End-to-end optimized image compression. In *International Conference of Learning Representations (ICLR)*, 2017.
- [3] J. Ballé, D. Minnen, S. Singh, S. J. Hwang, and N. Johnston. Variational image compression with a scale hyperprior. In *International Conference of Learning Representations (ICLR)*, 2018.
- [4] J. A. Benediktsson, J. A. Palmason, and J. R. Sveinsson. Classification of hyperspectral data from urban areas based on extended morphological profiles. *IEEE Transactions on Geoscience and Remote Sensing (TGRS)*, 43(3):480–491, 2005.
- [5] M. Biquard, M. Chabert, F. Genin, C. Latry, and T. Oberlin. Variational bayes image restoration with compressive autoencoders. *arXiv preprint arXiv:2311.17744*, 2023.
- [6] A. Bora, A. Jalal, E. Price, and A. G. Dimakis. Compressed sensing using generative models. In *International Conference on Machine Learning (ICML)*, 2017.
- [7] M. Bosch, C. M. Gifford, and P. A. Rodriguez. Super-resolution for overhead imagery using densenets and adversarial learning. In *2018 IEEE Winter Conference on Applications of Computer Vision (WACV)*, pages 1414–1422. IEEE, 2018.
- [8] J. Bégaïnt, F. Racapé, S. Feltman, and A. Pushparaja. CompressAI: a PyTorch library and evaluation platform for end-to-end compression research. *arXiv preprint arXiv:2011.03029*, 2020.
- [9] S. H. Chan, X. Wang, and O. A. Elgandy. Plug-and-play ADMM for image restoration: Fixed-point convergence and applications. *IEEE Transactions on Computational Imaging*, 3(1):84–98, 2016.
- [10] X. Chen, S. Xiang, C.-L. Liu, and C.-H. Pan. Vehicle detection in satellite images by hybrid deep convolutional neural networks. *IEEE Geoscience and remote sensing letters*, 11(10):1797–1801, 2014.
- [11] Z. Cheng, H. Sun, M. Takeuchi, and J. Katto. Learned image compression with discretized gaussian mixture likelihoods and attention modules. In *IEEE Conference on Computer Vision and Pattern Recognition (CVPR)*, 2020.
- [12] F. Chouteau, L. Gabet, R. Fraisse, T. Bonfort, B. Harnoufi, V. Greiner, M. Le Goff, M. Ortner, and V. Paveau. Joint super-resolution and image restoration for Pléiades Neo imagery. *The International Archives of the Photogrammetry, Remote Sensing and Spatial Information Sciences*, 43:9–15, 2022.

- [13] H. Chung, J. Kim, M. T. Mccann, M. L. Klasky, and J. C. Ye. Diffusion posterior sampling for general noisy inverse problems. In *International Conference on Learning Representations (ICLR)*, 2023.
- [14] J. Dean, G. Daras, and A. Dimakis. Intermediate layer optimization for inverse problems using deep generative models. In *NeurIPS 2020 Workshop on Deep Learning and Inverse Problems*, 2020.
- [15] M. Dhar, A. Grover, and S. Ermon. Modeling sparse deviations for compressed sensing using generative models. In *International Conference on Machine Learning (ICLR)*, pages 1214–1223. PMLR, 2018.
- [16] K. Ding, K. Ma, S. Wang, and E. P. Simoncelli. Image quality assessment: Unifying structure and texture similarity. *IEEE Transactions on Pattern Analysis and Machine Intelligence (TPAMI)*, 44(5):2567–2581, 2020.
- [17] G. Dorta, S. Vicente, L. Agapito, N. D. Campbell, and I. Simpson. Structured uncertainty prediction networks. In *IEEE Conference on Computer Vision and Pattern Recognition (CVPR)*, pages 5477–5485, 2018.
- [18] M. Duff, N. D. F. Campbell, and M. J. Ehrhardt. Regularising inverse problems with generative machine learning models. *Journal of Mathematical Imaging and Vision*, 2023.
- [19] M. A. Duff, I. J. Simpson, M. J. Ehrhardt, and N. D. Campbell. VAEs with structured image covariance applied to compressed sensing MRI. *Physics in Medicine & Biology*, 68(16):165008, 2023.
- [20] A. Durmus, E. Moulines, and M. Pereyra. Efficient bayesian computation by proximal Markov chain Monte Carlo: when Langevin meets Moreau. *SIAM Journal on Imaging Sciences*, 11(1):473–506, 2018.
- [21] M. Elad. *Sparse and Redundant Representations: From Theory to Applications in Signal and Image Processing*, volume 2. Springer, 2010.
- [22] G. Facciolo, C. De Franchis, and E. Meinhardt-Llopis. Automatic 3d reconstruction from multi-date satellite images. In *IEEE Conference on Computer Vision and Pattern Recognition (CVPR) Workshops*, pages 57–66, 2017.
- [23] J. Fu, Y. Liu, and F. Li. Single frame super resolution with convolutional neural network for remote sensing imagery. In *IEEE International Geoscience and Remote Sensing Symposium (IGARSS)*, pages 8014–8017. IEEE, 2018.
- [24] M. Galar, R. Sesma, C. Ayala, and C. Aranda. Super-resolution for sentinel-2 images. *The International Archives of the Photogrammetry, Remote Sensing and Spatial Information Sciences*, 42:95–102, 2019.
- [25] M. González, A. Almansa, and P. Tan. Solving inverse problems by joint posterior maximization with autoencoding prior. *SIAM Journal on Imaging Sciences*, 15(2):822–859, 2022.
- [26] I. J. Goodfellow, J. Pouget-Abadie, M. Mirza, B. Xu, D. Warde-Farley, S. Ozair, A. Courville, and Y. Bengio. Generative adversarial networks. *Communications of the ACM*, 2014.
- [27] J. Han, D. Zhang, G. Cheng, L. Guo, and J. Ren. Object detection in optical remote sensing images based on weakly supervised learning and high-level feature learning. *IEEE Transactions on Geoscience and Remote Sensing (TGRS)*, 53(6):3325–3337, 2014.
- [28] J. Ho, A. Jain, and P. Abbeel. Denoising diffusion probabilistic models. *Advances in Neural Information Processing Systems (NeurIPS)*, 2020.
- [29] M. Holden, M. Pereyra, and K. C. Zygalakis. Bayesian imaging with data-driven priors encoded by neural networks. *SIAM Journal on Imaging Sciences*, 15(2):892–924, 2022.
- [30] W. Huang, L. Xiao, Z. Wei, H. Liu, and S. Tang. A new pan-sharpening method with deep neural networks. *IEEE Geoscience and Remote Sensing Letters*, 12(5):1037–1041, 2015.
- [31] S. Hurault, A. Leclaire, and N. Papadakis. Gradient step denoiser for convergent plug-and-play. In *International Conference on Learning Representations (ICLR)*, 2022.
- [32] S. M. i Verdú, M. Chabert, T. Oberlin, and J. Serra-Sagrístà. Fixed-quality compression of remote sensing images with neural networks. *IEEE Journal of Selected Topics in Applied Earth Observations and Remote Sensing*, 2024.
- [33] K. Jiang, Z. Wang, P. Yi, G. Wang, T. Lu, and J. Jiang. Edge-enhanced GAN for remote sensing image superresolution. *IEEE Transactions on Geoscience and Remote Sensing (TGRS)*, 57(8):5799–5812, 2019.
- [34] Z. Kadkhodaie and E. Simoncelli. Stochastic solutions for linear inverse problems using the prior implicit in a denoiser. *Neural Information Processing Systems (NeurIPS)*, 34:13242–13254, 2021.
- [35] U. S. Kamilov, H. Mansour, and B. Wohlberg. A plug-and-play priors approach for solving nonlinear imaging inverse problems. *IEEE Signal Processing Letters*, 24(12):1872–1876, 2017.
- [36] B. Kawar, M. Elad, S. Ermon, and J. Song. Denoising diffusion restoration models. *Advances in Neural Information Processing Systems (NeurIPS)*, 35:23593–23606, 2022.
- [37] D. P. Kingma and P. Dhariwal. Glow: Generative flow with invertible 1x1 convolutions. 2018.
- [38] D. P. Kingma and M. Welling. Auto-encoding variational bayes. In *International Conference on Learning Representations (ICLR)*, 2014.
- [39] Z. Lai, K. Wei, and Y. Fu. Deep plug-and-play prior for hyperspectral image restoration. *Neurocomputing*, 481:281–293, 2022.
- [40] C. Latry, S. Fourest, and C. Thiebaud. Restoration technique for Pleiades-HR panchromatic images. *The International Archives of the Photogrammetry, Remote Sensing and Spatial Information Sciences*, 39:555–560, 2012.
- [41] R. Laumont, V. D. Bortoli, A. Almansa, J. Delon, A. Durmus, and M. Pereyra. Bayesian Imaging using plug & play priors: when Langevin meets Tweedie. *SIAM Journal on Imaging Sciences*, 15(2):701–737, 2022.

- [42] M. Lebrun, A. Buades, and J.-M. Morel. Implementation of the "Non-Local Bayes" (NL-Bayes) image denoising algorithm. *Image Processing On Line (IPOL)*, 3:1–42, 2013.
- [43] C. Ledig, L. Theis, F. Huszar, J. Caballero, A. Cunningham, A. Acosta, A. Aitken, A. Tejani, J. Totz, Z. Wang, and W. Shi. Photo-realistic single image super-resolution using a generative adversarial network. In *IEEE conference on Computer Vision and Pattern Recognition (CVPR)*, 2017.
- [44] J. Liang, J. Cao, G. Sun, K. Zhang, L. Van Gool, and R. Timofte. SwinIR: Image restoration using swin transformer. In *IEEE/CVF International Conference on Computer Vision (ICCV)*, pages 1833–1844, 2021.
- [45] L. Liebel and M. Körner. Single-image super resolution for multispectral remote sensing data using convolutional neural networks. *The International Archives of the Photogrammetry, Remote Sensing and Spatial Information Sciences*, 41:883–890, 2016.
- [46] P. Liu, J. Liu, and L. Xiao. A unified pansharpening method with structure tensor driven spatial consistency and deep plug-and-play priors. *IEEE Transactions on Geoscience and Remote Sensing (TGRS)*, 60:1–14, 2022.
- [47] A. Lugmayr, M. Danelljan, A. Romero, F. Yu, R. Timofte, and L. Van Gool. Repaint: Inpainting using denoising diffusion probabilistic models. In *IEEE/CVF Conference on Computer Vision and Pattern Recognition (CVPR)*, pages 11461–11471, 2022.
- [48] Z. Luo, F. K. Gustafsson, Z. Zhao, J. Sjölund, and T. B. Schön. Refusion: Enabling large-size realistic image restoration with latent-space diffusion models. In *IEEE/CVF Conference on Computer Vision and Pattern Recognition (CVPR)*, pages 1680–1691, 2023.
- [49] M. Makitalo and A. Foi. Optimal inversion of the generalized Anscombe transformation for Poisson-Gaussian noise. *IEEE Transactions on Image Processing (TIP)*, 22(1):91–103, 2012.
- [50] S. Mallat. Wavelet tour of signal processing: The sparse way, 2008.
- [51] J. Michel, J. Vinasco-Salinas, J. Inglada, and O. Hagolle. Sen2ven μ s, a dataset for the training of sentinel-2 super-resolution algorithms. *Data*, 7(7):96, 2022.
- [52] D. Minnen, J. Ballé, and G. D. Toderici. Joint autoregressive and hierarchical priors for learned image compression. In *Advances in neural information processing systems (NeurIPS)*, volume 31, 2018.
- [53] A. Mittal, A. K. Moorthy, and A. C. Bovik. No-reference image quality assessment in the spatial domain. *IEEE Transactions on Image Processing (TIP)*, 21(12):4695–4708, 2012.
- [54] D. Narnhofer, A. Habring, M. Holler, and T. Pock. Posterior-variance-based error quantification for inverse problems in imaging. *SIAM Journal on Imaging Sciences*, 17(1):301–333, 2024.
- [55] D. Pouliot, R. Latifovic, J. Pasher, and J. Duffe. Landsat super-resolution enhancement using convolution neural networks and Sentinel-2 for training. *Remote Sensing*, 10(3):394, 2018.
- [56] J. Prost, A. Houdard, A. Almansa, and N. Papadakis. Inverse problem regularization with hierarchical variational autoencoders. In *IEEE International Conference on Computer Vision (ICCV)*, 2023.
- [57] L. I. Rudin, S. Osher, and E. Fatemi. Nonlinear total variation based noise removal algorithms. *Physica D: Nonlinear Phenomena*, 1992.
- [58] O. Rybkin, K. Daniilidis, and S. Levine. Simple and effective VAE training with calibrated decoders. In *International Conference on Machine Learning (ICML)*, pages 9179–9189. PMLR, 2021.
- [59] L. Salgueiro Romero, J. Marcello, and V. Vilaplana. Super-resolution of Sentinel-2 imagery using generative adversarial networks. *Remote Sensing*, 12(15):2424, 2020.
- [60] H. Tao. Super-resolution of remote sensing images based on a deep plug-and-play framework. In *IEEE International Geoscience and Remote Sensing Symposium (IGARSS)*, pages 625–628. IEEE, 2020.
- [61] A. Teodoro, J. Bioucas-Dias, and M. Figueiredo. Sharpening hyperspectral images using plug-and-play priors. In *Latent Variable Analysis and Signal Separation: 13th International Conference*, pages 392–402. Springer, 2017.
- [62] R. Tibshirani. Regression shrinkage and selection via the lasso. *Journal of the Royal Statistical Society: Series B (Methodological)*, 1996.
- [63] A. Tikhonov. Solution of incorrectly formulated problems and the regularization method. *Soviet Math.*, 1963.
- [64] S. V. Venkatakrishnan, C. A. Bouman, and B. Wohlberg. Plug-and-play priors for model based reconstruction. *IEEE Global Conference on Signal and Information Processing (GlobalSIP)*, 2013.
- [65] X. Wang, J. Chen, and C. Richard. Tuning-free plug-and-play hyperspectral image deconvolution with deep priors. *IEEE Transactions on Geoscience and Remote Sensing (TGRS)*, 61:1–13, 2023.
- [66] X. Wang, K. Yu, S. Wu, J. Gu, Y. Liu, C. Dong, Y. Qiao, and C. Change Loy. ESRGAN: Enhanced super-resolution generative adversarial networks. In *European Conference on Computer Vision (ECCV) workshop*, pages 0–0, 2018.
- [67] Z. Wang, A. C. Bovik, H. R. Sheikh, and E. P. Simoncelli. Image quality assessment: from error visibility to structural similarity. *IEEE Transactions on Image Processing (TIP)*, 13(4):600–612, 2004.
- [68] Z. Wang, X. Cun, J. Bao, W. Zhou, J. Liu, and H. Li. Uformer: A general u-shaped transformer for image restoration. In *IEEE/CVF Conference on Computer Vision and Pattern Recognition (CVPR)*, pages 17683–17693, 2022.
- [69] X. Yang, Y. Ye, X. Li, R. Y. Lau, X. Zhang, and X. Huang. Hyperspectral image classification with deep learning models. *IEEE Transactions on Geoscience and Remote Sensing (TGRS)*, 56(9):5408–5423, 2018.
- [70] S. W. Zamir, A. Arora, S. Khan, M. Hayat, F. S. Khan, and M.-H. Yang. Restormer: Efficient transformer for

- high-resolution image restoration. In *IEEE/CVF Conference on Computer Vision and Pattern Recognition*, pages 5728–5739, 2022.
- [71] S. W. Zamir, A. Arora, S. Khan, M. Hayat, F. S. Khan, M.-H. Yang, and L. Shao. Multi-stage progressive image restoration. In *IEEE/CVF Conference on Computer Vision and Pattern Recognition*, pages 14821–14831, 2021.
- [72] J. Zhang, P. Zhong, Y. Chen, and S. Li. $l_{1/2}$ -regularized deconvolution network for the representation and restoration of optical remote sensing images. *IEEE Transactions on Geoscience and Remote Sensing (TGRS)*, 52(5):2617–2627, 2013.
- [73] K. Zhang, Y. Li, W. Zuo, L. Zhang, L. Van Gool, and R. Timofte. Plug-and-play image restoration with deep denoiser prior. *IEEE Transactions on Pattern Analysis and Machine Intelligence (TPAMI)*, 44(10):6360–6376, 2021.
- [74] K. Zhang, W. Zuo, Y. Chen, D. Meng, and L. Zhang. Beyond a gaussian denoiser: Residual learning of deep cnn for image denoising. *IEEE Transactions on Image Processing (TIP)*, 26:3142–3155, 2017.
- [75] K. Zhang, W. Zuo, S. Gu, and L. Zhang. Learning deep CNN denoiser prior for image restoration. In *IEEE conference on computer vision and pattern recognition (CVPR)*, pages 3929–3938, 2017.
- [76] K. Zhang, W. Zuo, and L. Zhang. Deep plug-and-play super-resolution for arbitrary blur kernels. In *IEEE/CVF Conference on Computer Vision and Pattern Recognition (CVPR)*, pages 1671–1681, 2019.
- [77] L. Zhang, J. Nie, W. Wei, Y. Li, and Y. Zhang. Deep blind hyperspectral image super-resolution. *IEEE Transactions on Neural Networks and Learning Systems*, 32(6):2388–2400, 2020.
- [78] R. Zhang, P. Isola, A. A. Efros, E. Shechtman, and O. Wang. The unreasonable effectiveness of deep features as a perceptual metric. In *IEEE/CVF Conference on Computer Vision and Pattern Recognition (CVPR)*, pages 586–595, 2018.
- [79] Y. Zhang, Y. Tian, Y. Kong, B. Zhong, and Y. Fu. Residual dense network for image super-resolution. In *IEEE Conference on Computer Vision and Pattern Recognition (CVPR)*, pages 2472–2481, 2018.
- [80] K. Zheng, L. Gao, D. Hong, B. Zhang, and J. Chanussot. NonRegSRNet: A nonrigid registration hyperspectral super-resolution network. *IEEE Transactions on Geoscience and Remote Sensing (TGRS)*, 60:1–16, 2021.
- [81] X. Zhu, H. Talebi, X. Shi, F. Yang, and P. Milanfar. Super-resolving commercial satellite imagery using realistic training data. In *2020 IEEE International Conference on Image Processing (ICIP)*, pages 498–502. IEEE, 2020.
- [82] Y. Zhu, K. Zhang, J. Liang, J. Cao, B. Wen, R. Timofte, and L. Van Gool. Denoising diffusion models for plug-and-play image restoration. In *IEEE/CVF Conference on Computer Vision and Pattern Recognition (CVPR)*, pages 1219–1229, 2023.